

소형 위성 바이오 탑재체를 위한 교차 간섭 없는 다중 센서 모듈

Crosstalk-free multi-sensor module for small satellite biological payloads

초록

지금까지의 소형 위성 생물학적 탑재체는 교차 간섭 없는 다중 센서 시스템 구축의 어려움으로 인해 pH, pNa, 용존 산소 함량 등을 모니터링할 수 없었고, 대부분 미생물의 성장만을 추적하는 흡광도 센서에만 의존해왔습니다. 이런 한계점을 해결하기 위해 본 연구는 각 센서의 작동 영역을 분리하여 교차 간섭 없는 이중 전기화학 pH 및 흡광도 센서 모듈을 성공적으로 개발하고 실험실에서 검증하였습니다. 개발된 센서 모듈은 레이저 절단한 아크릴 시트로 제작된 유체 카드, 패터닝된 전도성고분자/금속 pH 전극, 그리고 레이저-광저항기로 구성된 흡광도 센서를 사용하며 지구 저궤도에서의 효모 배양 및 모니터링 임무를 목적으로 개발되었습니다. pH 측정은 PANi-Ag/AgCl 전극을 사용하였고, 5 mW 650 nm 레이저와 CdS 광저항기를 이용하여 흡광도를 측정하였습니다. 먼저, 흡광도센서는 실리카 마이크로 구슬 용액으로, pH 센서는 소듐 아세테이트 완충용액을 사용하여 독립적으로 검증을 완료했습니다. 두 센서 간의 교차 간섭은 동시 작동 간섭 시험을 통해 확인했습니다. pH 5.9에서는 pH 센서의 출력이 1997 mV로 안정적이었고, 실리카 마이크로 구슬 농도가 증가함에 따라 흡광도는 0에서 1.078로 상승하였습니다. 반대로, 실리카 마이크로 구슬 농도를 일정하게 유지하고 pH를 조절하였을 때, 흡광도는 일정한 반면 pH 센서의 출력은 pH에 따라 선형적으로 변하였습니다. 두 경우 모두 각 센서가 서로 간섭 없이 동시에 작동하는 것을 확인하였습니다. 마지막으로, 이 센서 모듈을 활용해 실험실 환경에서 효모의 성장 및 pH 변화를 36시간 동안 성공적으로 모니터링하였으며 근미래 소형 위성 생물학적 탑재체의 계속 기능 개선에 응용될 것입니다.

Key Words: Small satellite payload; instrumentation; crosstalk-free; dual-configuration; electrochemical; optical

1. INTRODUCTION

To become a spacefaring civilization, it is essential to conduct biological experiments in space to understand how biological systems react to extra-terrestrial stimuli such as microgravity and radiation. Traditionally, most space-borne biology experiments are conducted on the International Space Station (ISS)^[1-4], a football-field sized orbital laboratory 400 km above ground in low Earth orbit (LEO). However, the ISS's continuous housing of multiple astronauts from different nations^[5] has various drawbacks, including high costs and prolonged development time due to safety regulations^[6], tight restrictions to experimental design for safety concerns^[7], as well as geopolitical circumstances that disrupt scientific activity on board^[8]. Moreover, pre-millennium attempts to incorporate instrumentation for studying biological systems within space vehicles predominantly involved singular non-scalable macro-sized (~cm) sensors such as glass probe-style open-circuit potential pH sensors and Clark type amperometric oxygen sensors^[9,10]. However, over the past few decades, significant advancements have been made in sensor fabrication and measurement capability, in addition to the development of more affordable and accessible space vehicle platforms.

Small satellites have become a capable but much more accessible option for conducting science in space^[6,11-14]. One of the most well-known and accessible small satellite platforms is the CubeSat, a specific type of small satellite made of multiple cubic modules, each with dimensions of 10 cm × 10 cm × 10 cm and weighs roughly under 2 kg^[15]. While this platform has a wide range of applications, this paper will focus on orbital laboratories with the purpose of studying microorganisms in space, as these microorganisms can play an important role in providing life-support to future crewed deep-space missions^[16-27]. Fig. 1 is a diagram of a potential autonomous orbital laboratory in LEO conducting microbial yeast cultivation and monitoring to study the effects of microgravity and space radiation on biological systems.

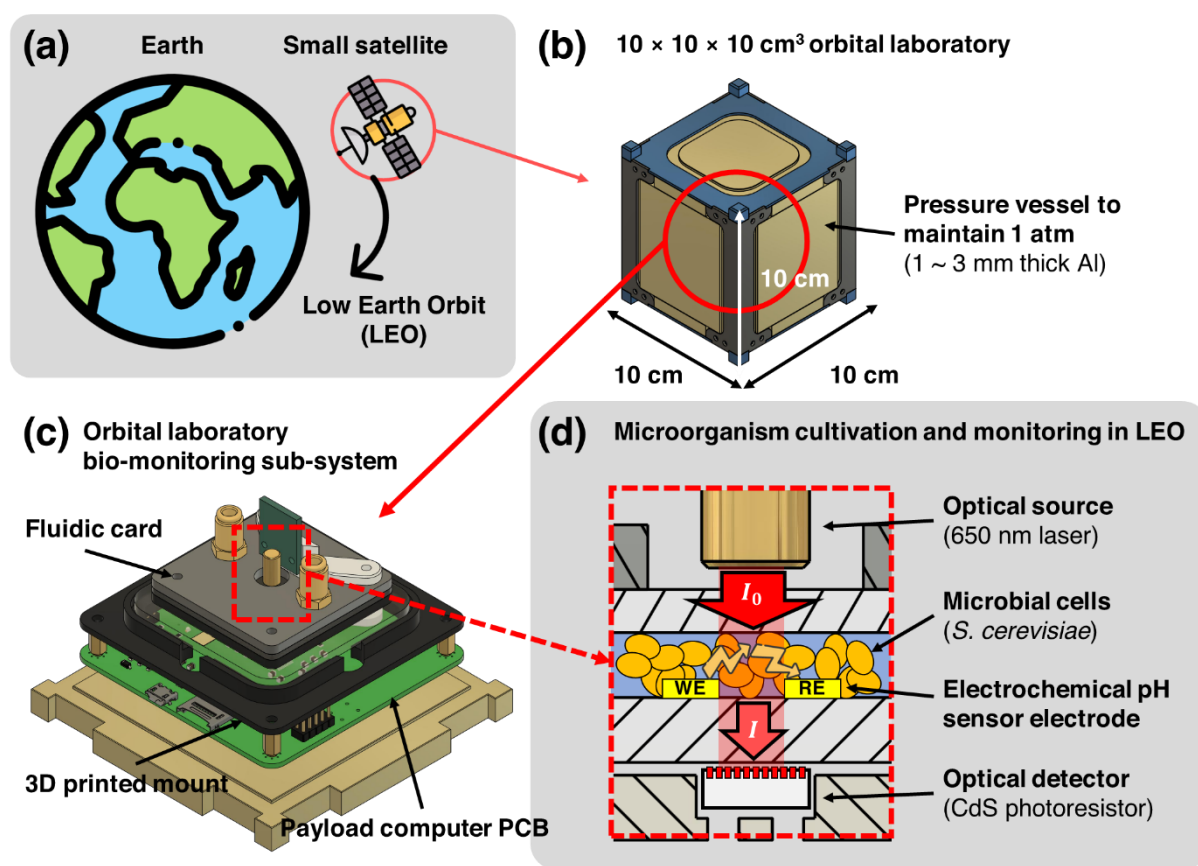


Fig. 1. Collection of diagrams depicting (a) a small satellite in Low Earth Orbit (LEO) (b) containing an orbital laboratory equipped (c) with a dual-configuration electrochemical and optical sensor module (d) capable of cultivating and monitoring microorganisms (e.g. yeast) in space.

Past examples of small satellite biological payloads designed to run experiments in orbit include the GeneSat-1^[28-30], PharmaSat 1^[31-33], O/OREOS^[34-38], EcAMSat^[39,40], and Biosentinel^[41-43]. Table 1 lists past CubeSat's with their target organisms and measurands. All the satellites had optical absorbance sensors for microbial growth tracking except for the SporeSat mission launched in 2014^[44] which had multiple Ca²⁺ ion sensitive electrodes and no optical absorbance sensors. While GraviSat^[45] claimed it had electrochemical ion-sensitive electrodes, its design, fabrication, or functional test results have not been reported in any detail. So far, those that have been reported in detail have had only one type of monitoring capability, optical or electrochemical, but never both.

Table 1. List of past CubeSats with bio-payloads and their organism and measurand.

Ref.	Year	CubeSat Name	Size	Organism	Measurand
[24-26]	2006	GeneSat-1	3U	<i>E. Coli</i>	Optical absorbance
[27-29]	2009	PharmaSat 1	3U	<i>S. cerevisiae</i>	Optical absorbance
[30-34]	2010	O/OREOS	3U	<i>B. Subtilis</i>	Optical absorbance
[40,55]	2014	SporeSat-1	3U	<i>Ceratomyces Richardii</i>	Calcium ions
[41]	Not launched	GraviSat	3U	Cyanobacteria/Algal Cultures	Optical absorbance
[40,55]	Not launched	SporeSat-2	3U	<i>Ceratomyces Richardii</i>	Optical absorbance
[35,36]	2017	EcAMSat	6U	<i>E. Coli</i>	Optical absorbance
[37-39]	2022	BioSentinel	6U	<i>S. cerevisiae</i>	Optical absorbance

Packing multiple sensor systems into a small volumetric footprint while maintaining clean I/O signals is challenging due to crosstalk from nearby sensors^[46,47]. One method to monitor both absorbance and pH during yeast cultivation is to use purely optical or purely electrochemical methods, as shown in Fig. 2a and Fig. 2b, respectively. An optical absorbance (a.k.a. optical density) sensor can monitor growth^[48], and an optical pH sensitive membrane can monitor pH^[49]. Alternatively, an electrochemical impedance spectroscopy sensor can monitor microbial growth^[50,51], and an electrochemical open-circuit potential pH sensor can monitor pH^[52]. These examples, however, suffer from potential crosstalk problems.

Specifically, in the case of a purely optical dual-sensor system, the yeast cells would interfere with the optical pH sensor by blocking the return radiation intensity (from the pH sensitive membrane) in addition to stray light from the optical source of the absorbance sensor and result in inaccurate pH readings^[53]. Similarly, a purely electrochemical dual-sensor system would have problems with the 3-electrode impedance spectroscopy-based growth sensor interfering with the open-circuit potential pH sensor^[46,54]. Specifically, the AC voltage applied across the impedance spectroscopy WE and RE would sink current through the open circuit potential WE and RE or induce an AC current in the OCP circuit through capacitive coupling or electromagnetic interference, thereby offsetting the measured OCP values which would result in false pH readings.

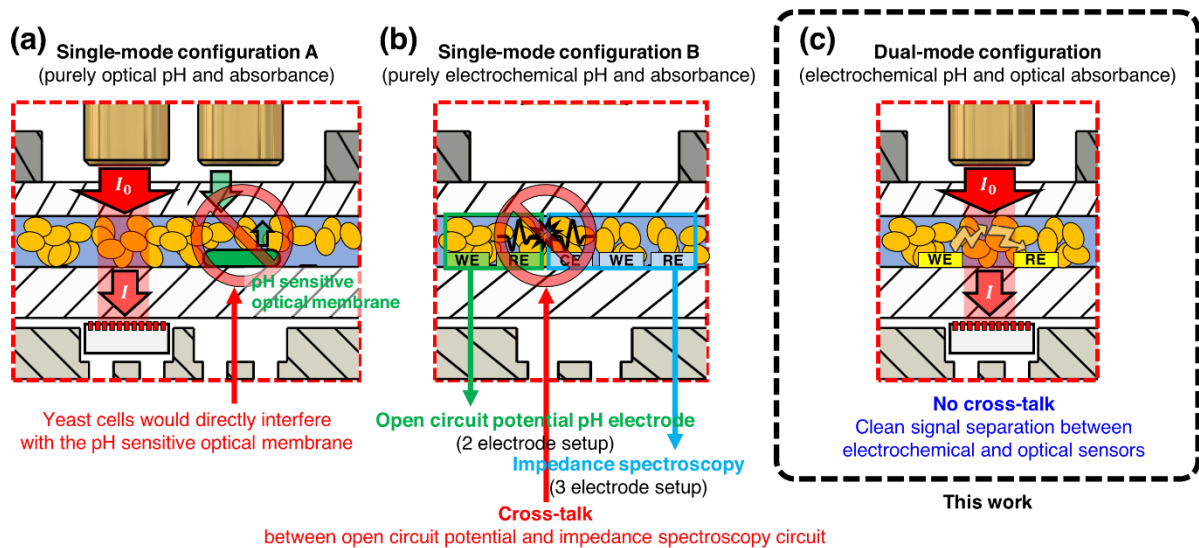


Fig. 2. Single-mode and dual-mode configurations for small satellite biological payload sensor module. Single-mode configuration for (a) purely optical pH and absorbance sensor system and (b) purely electrochemical pH and impedance-based absorbance sensor system. (c) Dual-mode configuration for electrochemical pH and optical absorbance sensor system.

Therefore, we have entirely split the operating domains of these sensors by having an optical absorbance sensor for growth monitoring and an electrochemical open circuit potential pH sensor as shown in Fig. 2c (dubbed dual-configuration). By splitting the operating domains of the sensor systems, inter-sensor crosstalk can be made essentially negligible. However, the complexity of the readout circuit could slightly increase as the dual-configuration sensor module would require two different readout circuits instead of one. This trade-off of a more complex readout circuit can be mitigated by simplifying overall circuit design, minimizing chip count to the bare necessity, and increasing the printed circuit board (PCB) layer count to combat board size increase if necessary.

We have designed, fabricated, and tested a laboratory benchtop prototype of a dual-configuration sensor module that incorporates both electrochemical and optical sensors. The module does not have the inherent crosstalk risks of a purely electrochemical or purely optical sensor system and is intended for possible future applications in small-satellite payloads. This dual-configuration sensor module will enable the simultaneous monitoring of a much wider set of measurands (not just limited to a single optical or electrochemical measurand) that were previously impossible

to measure within these small satellite payload laboratories.

2. MATERIALS AND METHODS

2.1. Materials, components, and equipment used

Laser cut PMMA (polymethyl methacrylate) sheets were used for the fluidic card. A 5-mW laser with peak emission at 650 nm was used as the optical source and a CdS photoresistor (GL55 series, Real Chance Co. Ltd., China) was used as the optical detector. Polyaniline (PANI) obtained from Merck KGaA (Germany) was used as the pH sensitive conducting polymer (as mentioned in our previous work^[52] and in several other publications). Ag/AgCl ink (Sun Chemical, United States) was used for the pH reference electrode (RE)^[55]. An STM32 L151C8Tx was used as the main microcontroller unit (MCU). Fusion360 (Autodesk, United States) was used to create the computer-generated 3D CAD models and the vector files for laser cutting the fluidic card. KiCad (Geneva, Switzerland) was used for designing the circuit schematics and PCB layout. The plastic mount for the laser was 3D modeled in Fusion360 and 3D printed using a Cubicon Single Plus (3DP-310F, HyVISION SYSTEM Inc., Seongnam-si, South Korea). Commercially available table sugar (sucrose), brewer's yeast (*Saccharomyces cerevisiae*, Baedaekam Instant Dry Yeast, Neulpureunn Co., Republic of Korea), and drinking water (Clover SD5CH Hot and Cold Dispenser, Sunshield Enterprise, Singapore) were used for yeast cultivation.

2.2. Design goals and constraints

The proposed dual-configuration electrochemical and optical sensor module has several basic mechanical and electrical design constraints that should be considered for it to be utilized in a future CubeSat payload (shown in Table 2). Note that biological CubeSat payloads are normally sealed within a 1 atm pressure and temperature-controlled vessel^[28-45], protecting the entire biological experimental module from any wild pressure or temperature swings. Therefore, the sensor module detailed in this paper will be designed assuming the pressure (1 atm) and temperature (25 ~ 30 °C) are maintained at a constant level.

Table 2. Mechanical and electrical design constraints for the developed dual-sensor module.

Category	Constraint	Specification	Unit
Mechanical	Volume	$< 8 \times 8 \times 8$	cm ³
Mechanical	Weight	< 2	kg
Electrical	Power consumption	< 2	W
Electrical	Operational voltage	< 3.6	V

Regarding volume, the pressure vessel for the bio-payload must maintain a 1 atm environment, limiting the volume available for the sensor module. Assuming a 1 cm wall thickness, the external sensor volume cannot exceed 8 cm × 8 cm × 8 cm within the 1U size constraint.

Regarding weight, a 1U CubeSat must weigh under 2 kg according to the CubeSat Design Specification revision 14 draft document^[15]. If the pressure vessel is made of 1 cm thick aluminum 7075 with a density of 2.81 g/cm³ and a total external volume of roughly 10 cm × 10 cm × 10 cm, it would weigh 1.371 kg. This leaves a maximum payload weight of 0.628 kg and hence the proposed dual sensor module must therefore weigh less than 0.628 kg.

Regarding power consumption, Clyde Space^[56] states that a basic 3 U CubeSat with 4 solar panels in LEO, on average, should have enough power for 60% of an orbit from one solar panel. With four 8 W solar panels, this means the CubeSat should have an average available power of 4.8 W per orbit. Assuming 0.4 W is used by non-payload related sub-systems, such as the ISIS On Board Computer (iOBC) from ISISPACE (Delft, Netherlands), we aim to keep payload power usage under 2 W while maintaining a minimum safety factor of 2 (margin for power budget). The payload will be designed to operate on 3.3 V as the nominal voltage of a single Li-ion cell is around 3.7 V.

2.3. Working principle

The dual-configuration sensor module consists of two sensors: 1) an optical absorbance sensor and an 2) electrochemical pH sensor. A 5-mW laser emits electromagnetic radiation (EMR) from the top optical source board, which passes through the multi-well fluidic card. This radiation intensity is partially attenuated due to absorption and scattering by suspended particles and is detected by the photoresistor on the bottom optical detector board. The PANi-Ag/AgCl pH sensitive electrode is placed within the well, with a hollow center to allow the laser to pass through. The device is shown in Fig. 3a (isometric view), Fig. 3b (cross-sectional diagram), Fig. 3c (exploded view), and Fig. 3d (photograph).

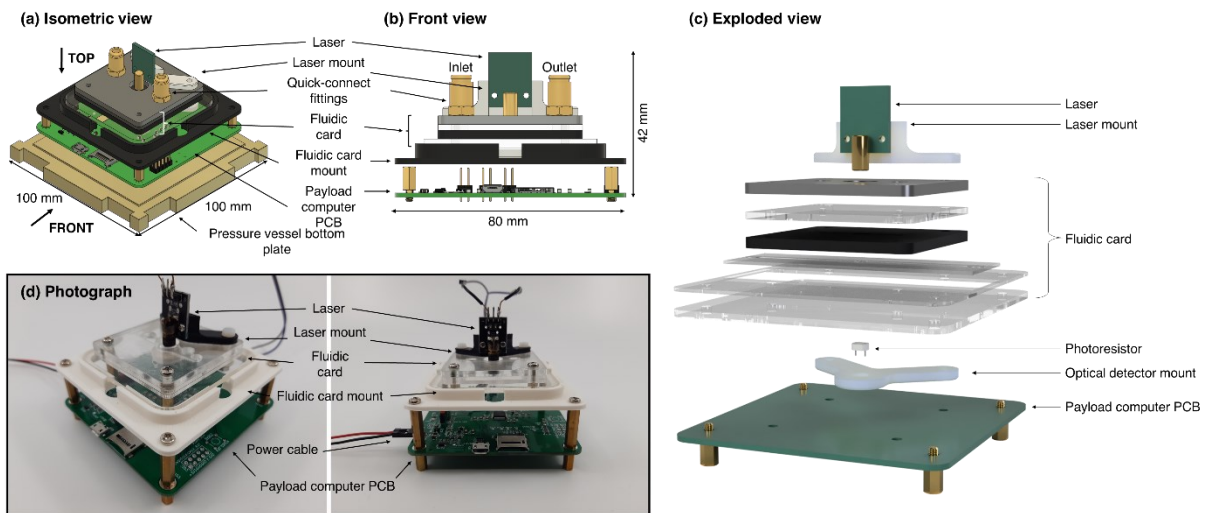


Fig. 3. CAD model and final photograph of the dual-configuration sensor module. (a) Isometric, (b) front, (c) exploded view of 3D model, and (d) photograph of the actual device.

Fig. 4a shows a system block diagram depicting the connections between all the payload components. The payload receives power from the CubeSat bus (in the non-payload section) and powers the MCU, memory, and the dual electrochemical and optical sensor module. The measured voltage obtained from each sensor's readout circuit is sent to the MCU and stored in memory. Periodically, the stored data in the memory would be processed by the payload computer MCU and sent to the On-Board Computer (OBC) on the CubeSat bus.

Fig. 4b shows the device in operation. Fig. 4c shows the top view of the absorbance sensor while Fig. 4d shows the laser light passing through the well containing target particles is attenuated and partially detected by the photoresistor. The photoresistor is connected to another resistor in series, acting as a voltage divider. As particle concentration changes, the light intensity passing through the well and arriving at the photoresistor changes, leading to a photoresistor resistance change, which results in a voltage change across the photoresistor. The voltage is detected by an instrumentation amplifier (INA) connected to a microcontroller GPIO pin.

Fig. 4e shows the top view of the circular PANi working electrode (WE) and Ag/AgCl reference electrode (RE) on a PMMA substrate. PANi is electrochemically polymerized on top of the Au WE base and becomes PANi/Au/Cr WE. Ag/AgCl ink is dropcast on top of Au RE base and becomes an Ag/AgCl/Au RE. The WE and RE are connected to an open-circuit potential (OCP) readout circuit that measures the potential difference between the WE and RE and sends it to the microcontroller.

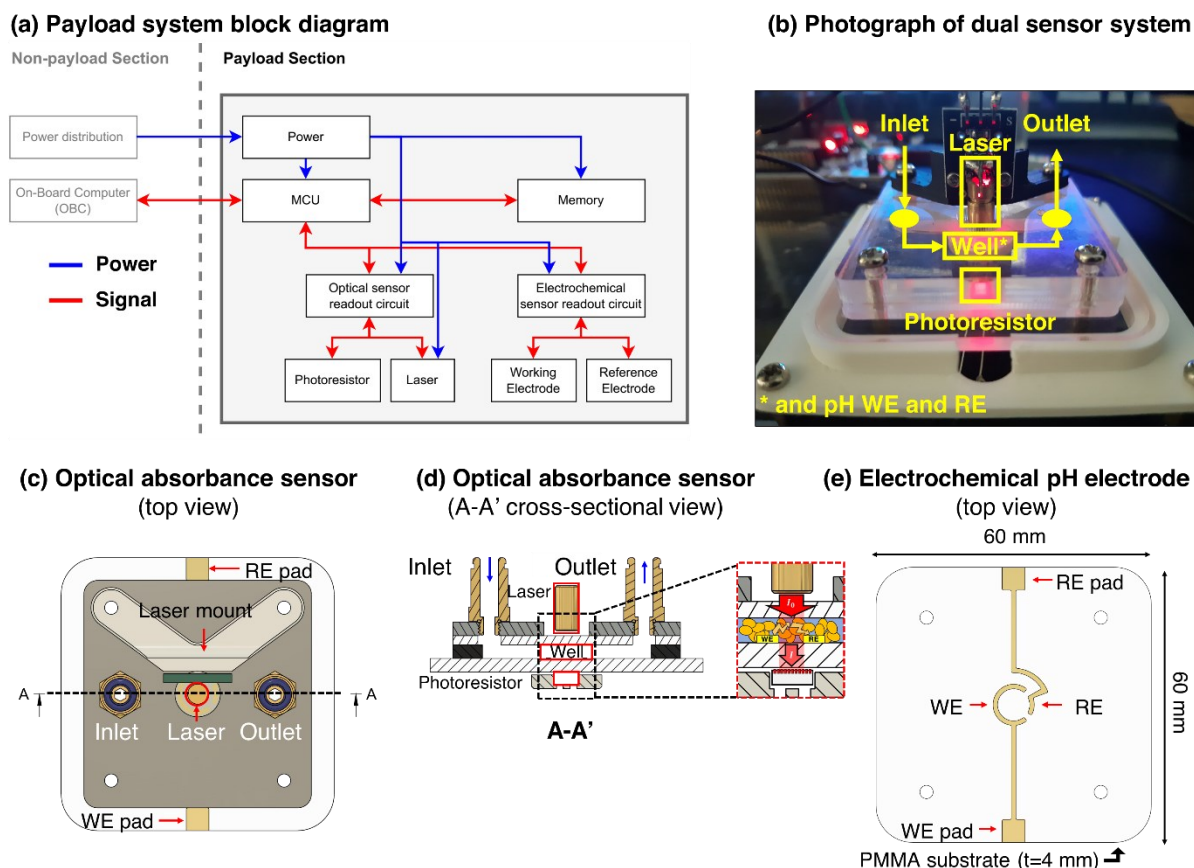


Fig. 4. (a) Payload system block diagram. (b) Photograph of dual-configuration sensor module. Optical absorbance sensor (c) top-view and (d) cross-section view. (e) Electrochemical pH sensor electrode top-view.

2.4. Fabrication and integration process

For the fluidic card fabrication process, the fluidic card combining the optical and electrochemical sensor was built up of multiple layers of laser-cut (30 W VLS 3.50, Universal Laser Systems) 2 ~ 3 mm thick PMMA sheets, as shown in Fig. 3c and Fig. 4d.

For the optical sensor fabrication process, a red 650 nm 5-mW laser and a CdS photoresistor were positioned on the top and bottom of the fluidic card with 3D printed mounts, respectively. Photoelectrical effects such as photoconductivity have been observed in PANi under short wavelength UVC (254 nm)^[61] light or strong ionizing γ -radiation ($< 10^{-6}$ nm)^[62]. Therefore, to minimize any kind of photoelectrical effects on the PANi WE the light utilized in our system was of low wattage (5 mW) and long wavelength (> 650 nm) near the infrared spectrum. Additionally, if necessary, these photoelectrical effects can further be mitigated by 1) temporally splitting the electrochemical and optical sensor operations so that the PANi membrane is only exposed to light for a minimal amount of time or 2) spatially locating the electrochemical electrode away from the light and thereby not expose the PANi to any light at all.

For the electrochemical sensor fabrication process, a 2 mm thick PMMA sheet (electrode substrate) was cleaned with soap water and dried with nitrogen blowing. Then, the PMMA sheet's top surface was treated with O₂ plasma for 35 s at 35 sccm for improved adhesion between the PMMA and upcoming metal layer. Next, a 250 μ m thick PMMA mask was bolted on top of the PMMA electrode layer. Then 20 nm Cr and 100 nm Au was vacuum deposited using an e-beam and thermal evaporator, respectively. To functionalize the electrodes, PANi was electropolymerized on top of the Au/Cr WE by cyclic voltammetry (CV) (from -0.2 V to 1 V vs. Ag/AgCl, 25 cycles) in 0.1 M aniline and 1 M HCl solution (CV plots shown in Fig. 7a and 7b). Finally, Ag/AgCl ink was applied on top

of the Au/Cr RE and dried for 2 h at 80°C to create an Ag/AgCl RE.

2.5. Circuit schematic and PCB layout

Detailed circuit schematics for each sensor readout circuit and the final payload computer PCB layout are shown in Fig. 5. Fig. 5a shows a top-down view of the payload computer PCB. Further circuit schematics for the power, memory, MCU, and sensors are shown in Fig. S1(a) ~S1(d) in the supplementary material.

As shown in Fig. 5b, the optical absorbance sensor is comprised of a 3.0 V 5-mW laser and a CdS photoresistor. The laser is connected to an electrical relay controlled by one of the MCU GPIOs. The photoresistor (R_x) and a 10 k Ω through-hole resistor are connected in a voltage divider configuration. The node between the 10 k Ω resistor and the CdS photoresistor is connected to a voltage follower and a low-pass filter (cut-off frequency at 7.9 Hz) which is in turn connected to MCU ADC channel 1. The voltage drop across the photoresistor is measured and used to find the resistance of the photoresistor.

For the electrochemical pH sensor readout circuit, detailed in Fig. 5c, an AD8223 instrumentation amplifier (INA) was used. The working electrode (WE) and reference electrode (RE) are connected to the inputs of the INA which is in turn again connected to MCU ADC channel 2. The open circuit potential between the WE and RE is measured and later converted to pH values. A default gain of 5 and offset of 1650 mV was set for the INA used for the electrochemical sensor readout circuit. This gain of 5 is used to make full use of the input voltage range (0 ~ 3.3 V) of the microcontroller unit within the relevant pH range (pH 4 ~ 6) and the 1650 mV offset exists to enable negative OCP measurements.

The entire module draws around 50 mA at 3.3 V (165 mW) without the laser. The laser (optical source of absorbance sensor) adds an additional 10 mA at 3 V (30 mW). Assuming constant laser usage, the entire dual sensor module uses 195 mW of power, which is well below the target 2 W power budget.

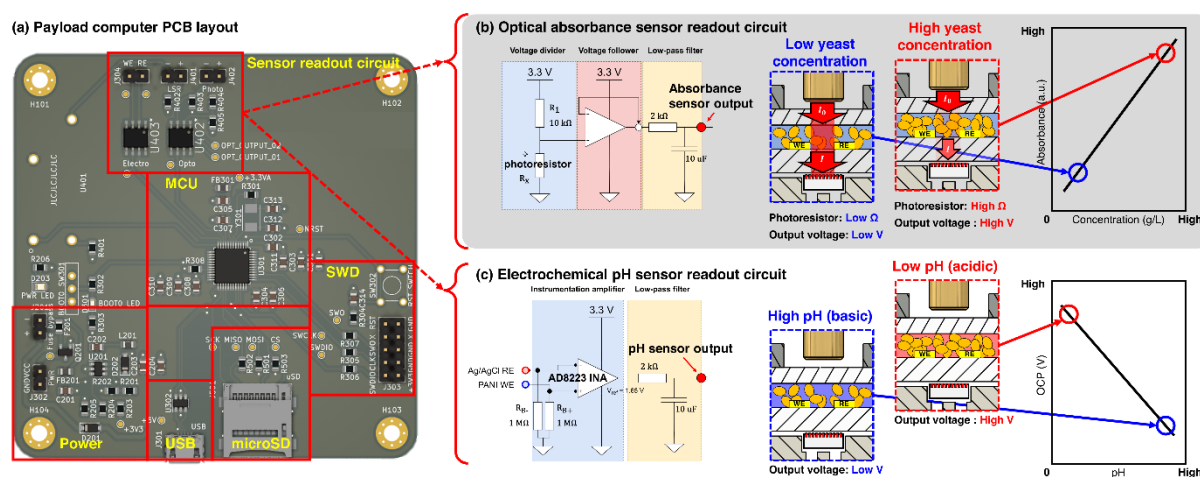


Fig. 5. (a) Payload computer PCB layout. Schematics for the (b) absorbance and (c) pH sensor readout circuits.

2.6. Silica microsphere suspension and pH buffer solution preparation

Dilutions of silica (SiO₂) microspheres with known diameter (9 ~ 13 μ m) and concentration (0 ~ 10 g/L) were prepared and used for the absorbance sensor characterization. Silica microspheres were used as model particles for their uniform absorbance spectrum and common usage as test particles for evaluating absorbance sensors. The microspheres were serially diluted in 10 mL of deionized (DI) water to create turbid liquid samples of silica microspheres with concentrations ranging from 0 to 10 g/L. The denser (higher concentration of silica microspheres) the microsphere suspension, the more turbid the sample is, resulting in higher absorbance.

Acetate buffers with pH ranging from 5.9 to 3.9 were prepared by mixing 0.1 M sodium acetate and 0.1 M acetic

acid in different proportions. The exact mixture proportions are given in Table S1 of the supplementary material. The pH values of these buffer solutions were confirmed using a commercial pH meter (SevenCompact S220 with pH accuracy of ± 0.002 , Mettler Toledo, USA).

2.7. Optical absorbance sensor characterization

First, the laser light source itself was characterized by establishing the relationship between the applied voltage and output light intensity. A smartphone light intensity sensor (GALAXY A30, Samsung, South Korea) was placed 13 mm away from the light source and the measurements were conducted in a dark room with ambient light intensity of 0 lux. Voltage ranging from 0 to 5 V was applied in 0.1 V intervals across the laser's positive and negative terminals. The equations describing transmittance and absorbance are shown in equations (1) and (2), respectively. Second, the relationship between measured voltage and photoresistor resistance is described in equation (3). Third, the relationship between photoresistor resistance value and light intensity is given by the GL55 photoresistor datasheet^[55] and the equation is detailed in equation (4). Finally, the absorbance plot of silica microspheres measured by the final absorbance sensor consisting of the light source, the fluidic card with liquid content, and the photoresistor, was obtained.

Absorbance gauges cell growth by measuring the change in light intensity before and after passing through the sample using Beer–Lambert's Law. A decrease in light intensity as the light passes through the sample correlates with higher biomass density. The relationship between measured absorbance and analyte concentration is described by Beer–Lambert's Law as

$$T(\%) = \left(\frac{I}{I_0}\right) \times 100 \quad (1)$$

$$A = \epsilon cl = \log_{10} \frac{I_0}{I} = \log_{10} \frac{100}{T} \quad (2)$$

where T is optical transmittance (%), I_0 is light intensity of incident light (or intensity of blank/reference solution), I is light intensity after passing through the sample (or with particle of interest within the blank/reference solution), A is light absorbance of the particles (in this case silica microspheres or yeast cells) (dimensionless), ϵ is molar attenuation coefficient ($M^{-1}cm^{-1}$), c is molar concentration (M), and l is optical path length (cm).

The absorbance level of silica (SiO_2) microspheres at concentrations ranging from 0 to 10 g/L were measured using the optical absorbance sensor. The voltage value V_0 was measured by the MCU ADC channel 1 (as shown in Fig. 3a). As a voltage divider setup, the resistance of the photoresistor is calculated as follows:

$$R = 10^4 \times V_0 / (3.3 - V_0) \quad (3)$$

where V_0 is the measured voltage drop across the photoresistor value in volts (V) and R is the photoresistor resistance in ohms (Ω).

The transfer function between the measured photoresistor resistance and light intensity is given as follows according to the datasheet^[57]:

$$I = 3.24358 \times 10^7 / R^{1.490} \quad (4)$$

where R is the photoresistor resistance in ohms (Ω) and I is the corresponding light intensity in lux.

To conduct the actual absorbance measurement, first, a reference liquid (DI water) with no particles was injected into the well and V_0 was measured. Then, the well was drained and V_0 was measured for all the concentrations of silica microspheres from 0 to 10 g/L. The measured voltage was used to calculate the photoresistor resistance using equation (3). Then the resistance was used to calculate the light intensity using equation (4). Finally, light was converted into transmittance and absorbance using equations (1) and (2), respectively. These measurements provide us with a typical absorbance (au) vs. concentration (g/L) curve as shown in Fig. 4c.

2.8. Electrochemical pH sensor characterization

To examine the performance of the electrochemical pH sensor, the open circuit potential values of varying acetate buffer solution (pH 5.9 ~ 3.9) were measured, using two different electrode configurations to cross-reference and confirm OCP values: 1) PANi-commercial Ag/AgCl RE (data shown Fig. 7c) and 2) PANi-custom Ag/AgCl RE (data shown Fig. 7d).

The acetate buffers were injected into the well through the inlet where the WE and RE were placed. The potential difference between WE and RE, labeled V_{OCP} in equation (5), were measured by the AD8223 INA and the resulting output voltage, labeled V_E in equation (5), was sent to the microcontroller board. These measurements provided us with an open circuit potential (V) vs. pH curve as shown in Fig. 7c and 7d.

The theoretical transfer function for the electrochemical pH readout circuit is shown in equation (5).

$$V_E = 5V_{OCP} + 1.65 \quad (5)$$

where V_E is the voltage output of the pH sensor readout circuit in volts and V_{OCP} is the open circuit potential between the WE and RE in volts (V). V_{OCP} is multiplied by 5 (the gain of the INA) and offset by 1.65 V (mid-supply voltage of 3.3 V and INA reference voltage) to enable the MCU ADC to measure negative V_{OCP} .

2.9. Combined absorbance and pH monitoring

To characterize the function of both the absorbance and pH sensor working simultaneously without significant crosstalk between the sensors, two different experiments were carried out.

First, pH was maintained at a uniform pH 5.952 while the absorbance of the solution was varied from 0.1 to 10.0 g/L (data shown in Fig. 8a). This was done by preparing six different solutions all at pH 5.952 but different concentrations of silica microspheres and measuring the pH and absorbance of each solution sample. 1 mL of solution was injected into the inlet using a pipette, measured for 5 minutes, and then sucked out of the channel and well using a pipette. To ensure a clean channel and well with no residue for the next solution sample, DI water was repeatedly injected in through the inlet and sucked through the outlet 5 times. Then to rid the channel and well of DI water residue and return the electrode surface to a dry state, a gentle steady stream of nitrogen gas was supplied for 5 seconds. This process was repeated in-between each new solution sample.

Second, absorbance was maintained at a stable 0.0 (0.0 g/L) while pH was varied from 5.9 to 3.9 (data shown in Fig. 8b). This was done by preparing six different solutions all at 0 g/L of silica microsphere concentration but different pH values and measuring the pH and absorbance of each solution sample. The process of cleaning the well and electrode surface in-between solution sample changes remained the same as from the previous paragraph.

2.10. Monitoring the growth and pH change of *S. cerevisiae* during yeast cultivation

Dry yeast pellets were retrieved from a dry -4°C refrigerator and allowed to thaw at room temperature ($23\text{--}25^{\circ}\text{C}$) over a period of 2 hours before being loaded into the fluidic chamber well. A total of 0.3 g of active dry yeast was placed in a 156 mm^3 cylindrical well. The yeast was grown by passing 1 mL of a growth medium containing 5 g of table sugar mixed with 50 mL of drinking water through the fluidic chamber well, which was then sealed using PI tape at the inlet and outlet. The device was incubated at 30°C in a 1 g laboratory environment, and automatic measurements were taken by the sensor every 1 second for 36 hours.

3. RESULTS AND DISCUSSION

3.1. Optical absorbance sensor characterization

Fig. 6 shows the light source output intensity, photoresistor response, and absorbance spectrum of the system and confirms the function of the optical absorbance sensor. The relationship between the applied voltage (V) and

laser intensity (lux) output is presented in Fig. 6a. The resistance (Ω) of the photoresistor according to light intensity (lux) is illustrated in Fig. 6b. Lastly, Fig. 6c displays the absorbance (au) vs. concentration (g/L) curve of micro-silica dilutions of varying concentrations. According to Fig. 6a, the 5-mW laser increased linearly in output intensity within the 3 ~ 5 V region, with a transfer function of $I = 1806V_{app} - 5580$ where V_{app} is the applied voltage (V) and I is the measured light intensity (lux).

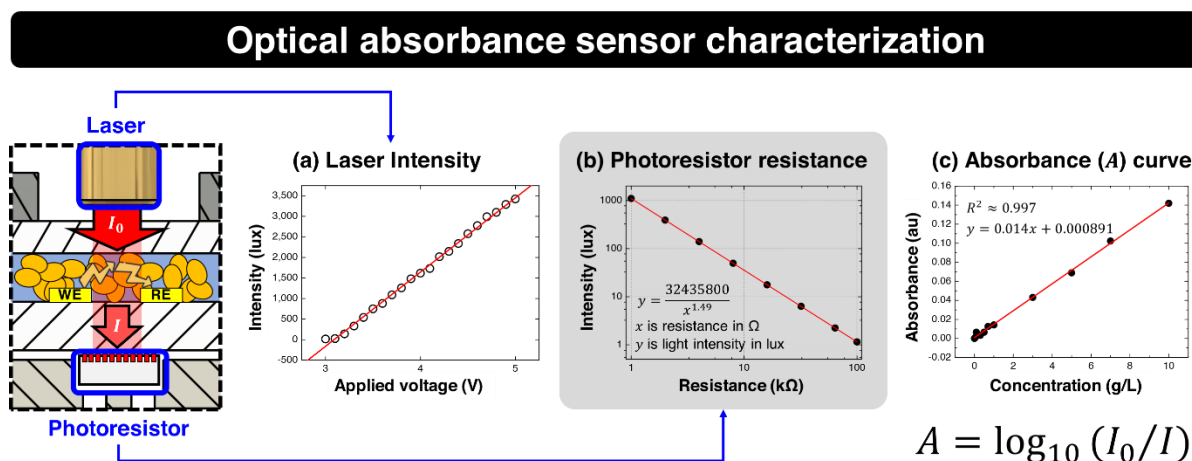


Fig. 6. Optical absorbance sensor characterization plots showing functioning absorbance sensor. (a) Applied voltage vs. intensity for laser characterization. (b) Intensity vs. resistance for photoresistor characterization. (c) Silica microsphere concentration vs. absorbance of optical absorbance sensor.

As for the photoresistor's response to light intensity, Fig. 6b shows the relationship between the photoresistor's resistance response to different light intensity levels, based on its datasheet. The intensity (lux) and resistance (Ω) share an inverse relationship with a transfer function of $I = (3.24358 \times 10^7)/R^{1.49}$ where R is the resistance (Ω) and I is the measured light intensity (lux).

Finally, Fig. 6c shows a remarkably linear relationship between actual micro-silica particle concentration (g/L) and measured absorbance (au) with a transfer function of $A = 0.014c - 0.000891$ ($R^2 \approx 0.997$) where c is the concentration (g/L) and A is the measured absorbance (au).

Fig. 6a and 6b show that the laser and photoresistor making up the optical absorbance sensor are predictable and characterizable. This enables us to establish a relationship between the measured absorbance and actual concentration of the micro-silica particles under investigation (shown in Fig. 6c).

3.2. Electrochemical pH sensor characterization

The characterization plots for the electrochemical pH sensor are shown in Fig. 7. Fig. 7a shows a 2D diagram of the placement of the PANi WE and Ag/AgCl RE within the well and a visual depiction of the open circuit potential (the potential difference between the WE and RE). The electrodes are placed apart so that the radiation has an optically clear path from the laser at the top all the way down to the photodetector.

Fig. 7b shows the CV plot of the WE during PANi electropolymerization. As CV cycle increased from 0 to 25 cycles, peak current values increased from 0 mV to 3.5 mV. A total of four current peaks (labeled peak α , β , α^* , β^* in Fig. 7b) that are well known and previously reported^[60] were observed. Peak α is an oxidation peak where leucoemeraldine (fully reduced form of PANi) is oxidized to emeraldine (half-reduced form of PANi). Peak β is attributed to the oxidation of emeraldine to pernigraniline (fully oxidized PANi). Peak β^* represents the reduction of pernigraniline to emeraldine and peak α^* is assigned to the reduction of emeraldine to leucoemeraldine. Therefore, the resulting CV plot and these peaks show the successful electropolymerization of PANi and therefore the fabrication of PANi/Au/Cr WE.

Fig. 7c and 7d are open-circuit potential measurement plots of PANi-commercial Ag/AgCl and PANi-custom

Ag/AgCl RE respectively, both measured using the developed custom payload computer. Both show the x -axis as pH and the y -axis as open-circuit potential (OCP) values between the WE and RE for PANi-commercial Ag/AgCl and PANi-custom Ag/AgCl electrodes respectively. As expected, in both circumstances, as pH was decreased from 5.9 to 3.9 and became more acidic, the measured OCP values increased. For the commercial Ag/AgCl RE, the OCP increased from 2573.0 mV to 3102.8 and the linear regression function was $y = -255.6x + 4103$ ($R^2 \approx 0.941$). For the custom Ag/AgCl RE, the OCP increased from 2685.0 mV to 3374.3 and the linear regression function was $y = -344.6x + 4718.2$ ($R^2 \approx 0.971$). In both cases, the x was pH (pH) and y was measured OCP (V) between PANi WE and Ag/AgCl RE. The slight difference in sensitivity between the commercial Ag/AgCl and custom Ag/AgCl RE could be attributed to the absence of a salt-bridge (i.e. 3.5 M NaCl or KCl filling solution) on the custom Ag/AgCl RE. This could result in a non-constant potential change from the Ag/AgCl RE and therefore in the increase of OCP between the WE and RE, contributing to a slight increase in sensitivity further amplified by the high gain of the readout circuit. However, a low relative standard deviation (RSD) for each data point ($< 0.78\%$) and an R^2 value of 0.971 indicates good reproducibility and strong correlation between pH and measured OCP and is completely suitable for the purposes of establishing a relationship between measured OCP and actual pH values.

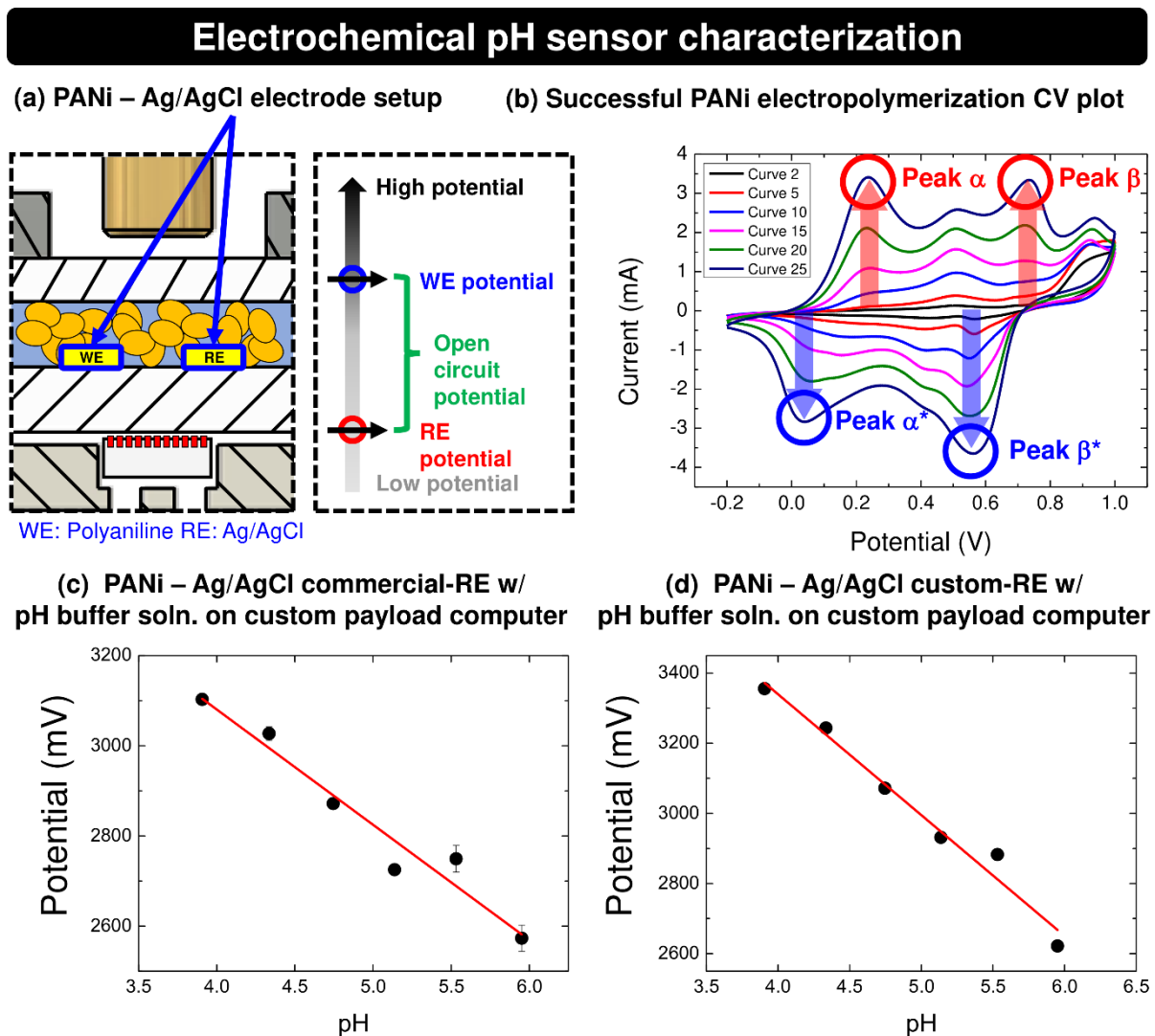


Fig. 7. Electrochemical pH sensor characterization plots. (a) Side drawing of the internal well and electrochemical pH sensor WE and RE placement. (b) CV plot during electropolymerization in 0.1 M aniline and 1.0 M HCl. OCP vs. pH plot of (c) PANi WE – commercial Ag/AgCl RE and (d) PANi WE – custom Ag/AgCl RE.

To summarize, Fig. 7 indicates that the electrochemical pH sensor comprised of a PANi WE and an Ag/AgCl RE with a custom OCP measuring readout circuit could accurately measure the pH of a liquid sample within the pH range of 5.9 to 3.9. The final sensor displayed a sensitivity of -344.6 mV/pH (with a gain of 5) and a minimum linear range of pH 4 to 6. It is worth noting that without gain (gain set to 1), the sensitivity would be -68.9 mV/pH and this value has been validated through previous research^[52]. Thus, this electrochemical pH sensor is suitable for monitoring pH fluctuations during yeast fermentation and can also function as an instrument onboard an autonomous orbital laboratory.

3.3. Combined absorbance and pH monitoring

Fig. 8 depicts the simultaneous measurement output of the absorbance sensor and the pH sensor. In Fig. 8a, the pH was maintained at a constant level (pH 5.952) while the absorbance was increased by increasing the silica microsphere concentration from 0 to 10 g/L. The OCP measurements were 1997.9 ± 47.0 mV (average \pm standard deviation) ($n = 6$), and the absorbance increased from 0 at 0 g/L to 1.078 at 10 g/L with a linear regression fit equation of $y = 0.1127x + 0.00639$ ($R^2 = 0.972$).

In Fig. 8b, the absorbance was maintained at a constant level while the pH was lowered from 5.9 to 3.9. The absorbance measurements were 0.002 ± 0.006 ($n = 6$), while the OCP increased from 1898.1 mV at pH 5.9 to 2473.7 mV at pH 3.9 with a linear regression fit equation of $y = -267.1x + 3551.8$ ($R^2 = 0.892$).

Fig. 8a and 8b combined show that the optical absorbance sensor and electrochemical pH sensor can both operate independently at the same time without inter-sensor crosstalk.

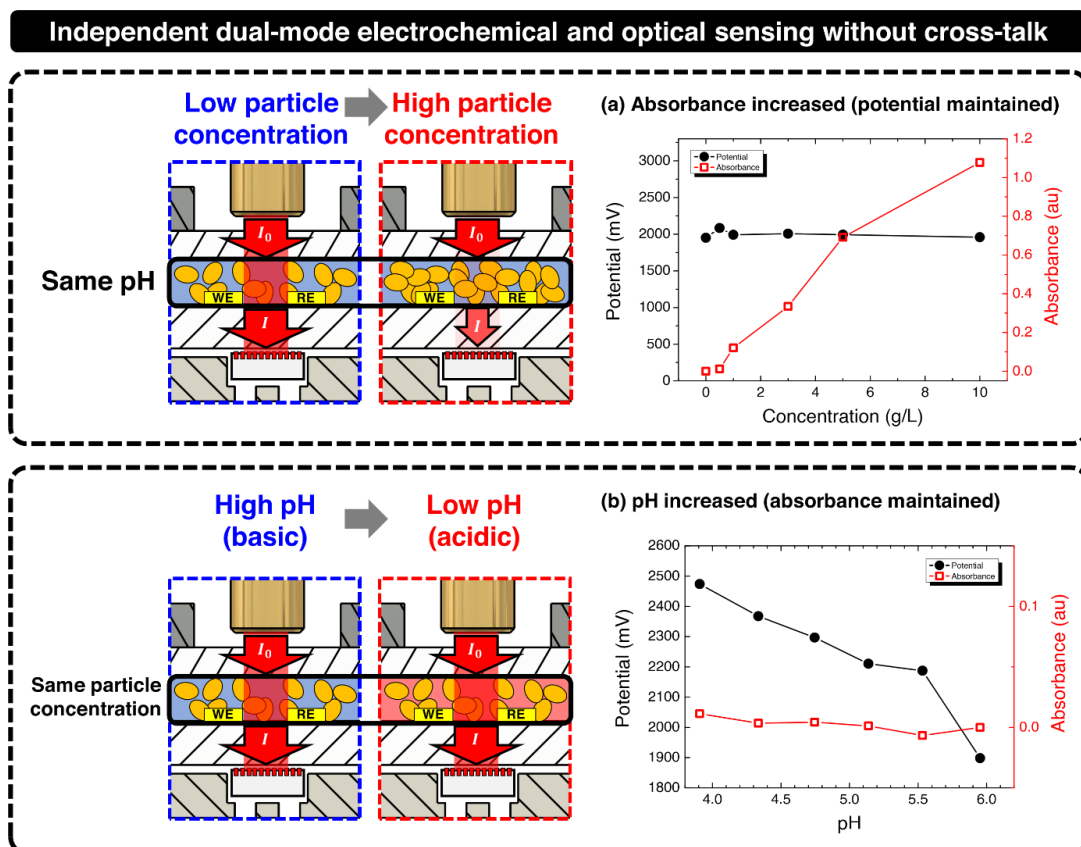


Fig. 8. Dual-configuration output while running both sensors simultaneously without cross-talk. (a) pH was maintained at pH 5.952 and micro-silica particle concentration was increased from 0 to 10 g/L. (b) Micro-silica particle concentration was maintained at 0 g/L and pH was decreased from pH 5.9 to 3.9.

3.4. Monitoring the growth and pH change of *S. cerevisiae* during yeast cultivation

The developed dual-sensor module was utilized to simultaneously monitor pH and absorbance changes in *S. cerevisiae* cultivation over 36 hours. As demonstrated in Fig. 9a, the absorbance increased from 0.3 to 0.8, consistent with the growth in size and number of yeast cells, which resulted in decreased light penetration through the fluidic well and increased absorbance. Conversely, Fig. 9b illustrates a decrease in pH from 7.5 to 4.0, indicating increased acidity. This decrease can be explained by the absorption of basic amino acids and primary phosphate, excretion of organic acid, and dissolution of CO_2 ^[58].

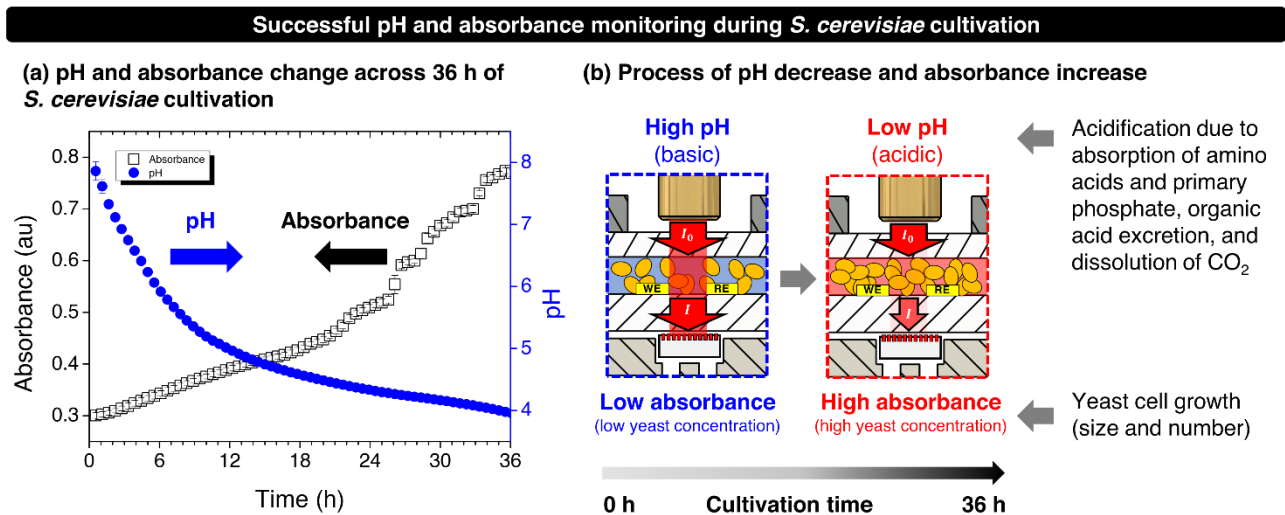


Fig. 9. Successful monitoring of *S. cerevisiae* cultivation using dual-configuration electrochemical pH and optical absorbance sensor. (a) Time-series pH and absorbance value change across 36 h of yeast cultivation. (b) Diagram explaining the process behind acidification (pH decrease) and cell growth (absorbance increase) during yeast cultivation.

3.5. Adherence to design goals and constraints

The developed dual-configuration sensor module has met all design constraints outlined in this paper. The dual-configuration electrochemical and optical sensor module is $80 \times 80 \times 42 \text{ mm}^3$ (268.8 mL) in volume and weighs 1.471 kg (the payload without the pressure vessel weighs just 100 g, and the pressure vessel weighs 1.371 kg), which is well below the $80 \times 80 \times 80 \text{ mm}^3$ (512 mL) and 2 kg volume and weight budget. As for electrical constraints, at constant power usage the sensor module consumes 0.195 W of power at 3.3 V, which is well under the 2 W power budget operating at a maximum of 3.6 V.

4. CONCLUSION

To conclude, this paper has reported the development and testing of a crosstalk-free dual-configuration electrochemical and optical pH and absorbance sensor module suitable for future small satellite biological payloads. The compact size of the dual-configuration optical and electrochemical sensor module, measuring only $80 \times 80 \times 42 \text{ mm}^3$, weighing 100 g, and consuming 0.195 W of power, could monitor the absorbance and pH change of silica microspheres, acetate buffer solution, and *S. cerevisiae* cultivation for a period of 36 hours. The design, fabrication, and testing methods of this dual-configuration sensor module have been thoroughly explained and can be used as a reference for future development of small satellite biological payloads. For actual implementation of this dual-configuration sensor module design in a small satellite mission, we are currently working on a scaled-up version of the sensor module complete with a multi-well fluidic card and a compact onboard payload computer while maintaining similar payload volume, weight, and power consumption constraints as outlined in this paper.

참고문헌

- [1] P. Baglioni, M. Sabbatini, G. Horneck, *Astrobiology Experiments in Low Earth Orbit: Facilities, Instrumentation, and Results*, in: G. Horneck, P. Rettberg (Eds.), *Complete Course in Astrobiology*, Wiley-VCH Verlag GmbH & Co. KGaA, Weinheim, Germany, 2007: pp. 273–319. <https://doi.org/10.1002/9783527618996.ch11>.
- [2] G. Horneck, D.M. Klaus, R.L. Mancinelli, *Space Microbiology*, *Microbiology and Molecular Biology Reviews*. 74 (2010) 121–156. <https://doi.org/10.1128/MMBR.00016-09>.
- [3] A. Paul, R.M. Wheeler, H.G. Levine, R.J. Ferl, *Fundamental Plant Biology Enabled by The Space Shuttle*, *American J of Botany*. 100 (2013) 226–234. <https://doi.org/10.3732/ajb.1200338>.
- [4] F. Ferranti, M. Del Bianco, C. Pacelli, *Advantages and Limitations of Current Microgravity Platforms for Space Biology Research*, *Applied Sciences*. 11 (2020) 68. <https://doi.org/10.3390/app11010068>.
- [5] M. Garcia, *Crews and Expeditions*, NASA International Space Station. (2023). http://www.nasa.gov/mission_pages/station/expeditions/index.html (accessed March 4, 2023).
- [6] A. Poghosyan, A. Golkar, *CubeSat evolution: Analyzing CubeSat capabilities for conducting science missions*, *Progress in Aerospace Sciences*. 88 (2017) 59–83. <https://doi.org/10.1016/j.paerosci.2016.11.002>.
- [7] Santo, L., Quadri, F., Ganga, P. L., & Zolesi, V. (2015). Mission BION-M1: Results of RIBES/FOAM2 experiment on shape memory polymer foams and composites. *Aerospace Science and Technology*, 40, 109–114. <https://doi.org/10.1016/j.ast.2014.11.008>
- [8] M. Smith, *Russia Suspends Some Space Cooperation with U.S., Europe*, (2022). <https://spacepolicyonline.com/news/russia-suspends-some-space-cooperation-with-u-s-europe/> (accessed February 28, 2023).
- [9] Oelpner, W., Herrmann, S., & Kaden, H. (1997). *Electrochemical Sensors and Sensor Module for Studying Biological Systems in Space Vehicles*. In *Aerospace Science and Technology* (Vol. 4).
- [10] B. H. Weigl, W. Trettnak, A. Holobar, I. Klimant, W. Gruber, R. Hager, R. Benes, P. O'Leary, (1994). Determination of pH, oxygen and carbon dioxide in microgravity bioreactors with emphasis on application in BIOST (Bioprocessing Space Technology). In *Life Sciences Research in Space, Proceedings of the Fifth European Symposium held 26 September – 1 October, 1993 in Arcachon, France*. Edited by H. Oser and T.D. Guyenne. ESA SP-366. European Space Agency, 1994., p.473
- [11] I. Mateos, R. Sánchez-Mínguez, J. Ramos-Castro, *Design of a CubeSat payload to test a magnetic measurement system for space-borne gravitational wave detectors*, *Sensors and Actuators, A: Physical*. 273 (2018) 311–316. <https://doi.org/10.1016/j.sna.2018.02.040>.
- [12] D. Seo, J. Jeong, T. Kim, J. Lee, *A MEMS glass membrane igniter for improved ignition delay and reproducibility*, *Sensors and Actuators A: Physical*. 258 (2017) 22–31. <https://doi.org/10.1016/j.sna.2017.02.011>.
- [13] F. Qiu, J. Wang, Y. Zhang, G. Yang, C. Weng, *Resolution limit of anisotropic magnetoresistance(AMR) based vector magnetometer*, *Sensors and Actuators A: Physical*. 280 (2018) 61–67. <https://doi.org/10.1016/j.sna.2018.07.031>.
- [14] M.A.C. Silva, D.C. Guerrieri, H. van Zeijl, A. Cervone, E. Gill, *Vaporizing Liquid Microthrusters with integrated heaters and temperature measurement*, *Sensors and Actuators A: Physical*. 265 (2017) 261–274. <https://doi.org/10.1016/j.sna.2017.07.032>.
- [15] California Polytechnic State, *Cubesat design specification*, The CubeSat Program, California Polytechnic. 14 (2020) 34.
- [16] Y. Liu, C.S. Cockell, G. Wang, C. Hu, L. Chen, R. De Philippis, *Control of Lunar and Martian Dust—Experimental Insights from Artificial and Natural Cyanobacterial and Algal Crusts in the*

- Desert of Inner Mongolia, China, *Astrobiology*. 8 (2008) 75–86. <https://doi.org/10.1089/ast.2007.0122>.
- [17] I.I. Brown, S. Sarkisova, Bio-Weathering of Lunar and Martian Rocks by Cyanobacteria: A Resource for Moon and Mars Exploration, *Lunar and Planetary Sciences XXXIX*. (2008) 1–2.
- [18] G. Murukesan, H. Leino, P. Mäenpää, K. Ståhle, W. Raksajit, H.J. Lehto, Y. Allahverdiyeva-Rinne, K. Lehto, Pressurized Martian-Like Pure CO₂ Atmosphere Supports Strong Growth of Cyanobacteria, and Causes Significant Changes in their Metabolism, *Origins of Life and Evolution of Biospheres*. 46 (2016) 119–131. <https://doi.org/10.1007/s11084-015-9458-x>.
- [19] C. Verseux, M. Baqué, K. Lehto, J.P.P. De Vera, L.J. Rothschild, D. Billi, Sustainable life support on Mars – The potential roles of cyanobacteria, *International Journal of Astrobiology*. 15 (2016) 65–92. <https://doi.org/10.1017/S147355041500021X>.
- [20] T. Niederwieser, P. Kocielek, D. Klaus, Spacecraft cabin environment effects on the growth and behavior of *Chlorella vulgaris* for life support applications, *Life Sciences in Space Research*. 16 (2018) 8–17. <https://doi.org/10.1016/j.lssr.2017.10.002>.
- [21] L. Qin, Q. Yu, W. Ai, Y. Tang, J. Ren, S. Guo, Response of cyanobacteria to low atmospheric pressure, *Life Sciences in Space Research*. 3 (2014) 55–62. <https://doi.org/10.1016/j.lssr.2014.09.001>.
- [22] D. Billi, M. Baqué, C. Verseux, L. Rothschild, J.P. de Vera, Desert cyanobacteria: Potential for space and earth applications, 2017. https://doi.org/10.1007/978-3-319-48327-6_6.
- [23] H.D. Smith, M. Baqué, A.G. Duncan, C.R. Lloyd, C.P. McKay, D. Billi, Comparative analysis of cyanobacteria inhabiting rocks with different light transmittance in the Mojave Desert: A Mars terrestrial analogue, *International Journal of Astrobiology*. 13 (2014) 271–277. <https://doi.org/10.1017/S1473550414000056>.
- [24] D. Billi, M. Baqué, H.D. Smith, C.P. McKay, Cyanobacteria from Extreme Deserts to Space, *Advances in Microbiology*. 3 (2013) 80–86. <https://doi.org/10.4236/aim.2013.36A010>.
- [25] M.M. Cohen, M.T. Flynn, R.L. Matossian, Water Walls Life Support Architecture, 43rd International Conference on Environmental Systems. (2013) 1–15. <https://doi.org/10.2514/6.2013-3517>.
- [26] E.D. Revellame, R. Aguda, A. Chistoserdov, D.L. Fortela, R.A. Hernandez, M.E. Zappi, Microalgae cultivation for space exploration: Assessing the potential for a new generation of waste to human life-support system for long duration space travel and planetary human habitation, *Algal Research*. 55 (2021) 102258. <https://doi.org/10.1016/j.algal.2021.102258>.
- [27] Belz, S., Ganzer, B., Messerschmid, E., Friedrich, K. A., & Schmid-Staiger, U. (2013). Hybrid life support systems with integrated fuel cells and photobioreactors for a lunar base. *Aerospace Science and Technology*, 24(1), 169–176. <https://doi.org/10.1016/j.ast.2011.11.004>
- [28] C. Kitts, J. Hines, E. Agasid, A. Ricco, B. Yost, M. Karolyn Ronzano, J. Puig-Suari, The GeneSat-1 Microsatellite Mission: A Challenge in Small Satellite Design, *Proceedings of the AIAA/USU Conference on Small Satellites*. (2006) 1–6. <https://doi.org/SSC06-IV-8>.
- [29] G. Minelli, C. Kitts, K. Ronzano, C. Beasley, R. Rasay, I. Mas, P. Williams, P. Mahacek, J. Shepard, J. Acain, J. Hines, E. Agasid, C. Friedericks, M. Piccini, M. Parra, L. Timucin, M. Henschke, E. Luzzi, N. Mai, M. McIntyre, R. Ricks, D. Squires, C. Storment, J. Tucker, B. Yost, G. Defouw, A. Ricco, Extended Life Flight Results from the GeneSat-1 Biological Microsatellite Mission, *USU Conference on Small Satellites*. (2008) 1–10. <https://doi.org/SSC08-II-4>.
- [30] C. Kitts, K. Ronzano, R. Rasay, I. Mas, P. Williams, P. Mahacek, G. Minelli, J. Hines, E. Agasid, C. Friedericks, M. Piccini, M. Parra, L. Timucin, C. Beasley, M. Henschke, E. Luzzi, N. Mai, M. McIntyre, R. Ricks, D. Squires, C. Storment, J. Tucker, B. Yost, G. Defouw, A. Ricco, Flight Results from the GeneSat-1 Biological Microsatellite Mission, 2007 AIAA Small Satellite Conference. (2007) 1–11. <https://doi.org/SSC08-II-4>.
- [31] A.J. Ricco, M. Parra, D. Niesel, M. McGinnis, D. Ly, A. Kudlicki, J.W. Hines, M. Piccini, L.

- Timucin, C. Beasley, R. Ricks, M. McIntyre, PHARMASAT: DRUG DOSE DEPENDENCE RESULTS FROM AN AUTONOMOUS MICROSYSTEM-BASED SMALL SATELLITE IN LOW EARTH ORBIT, in: 2010 Solid-State, Actuators, and Microsystems Workshop Technical Digest, Transducer Research Foundation, San Diego, 2010: pp. 110–113. <https://doi.org/10.31438/trf.hh2010.31>.
- [32] A.J. Ricco, M. Parra, D. Niesel, M. Piccini, D. Ly, M. McGinnis, A. Kudlicki, J.W. Hines, L. Timucin, C. Beasley, R. Ricks, M. McIntyre, C. Friedericks, M. Henschke, R. Leung, M. Diaz-Aguado, C. Kitts, I. Mas, M. Rasay, E. Agasid, E. Luzzi, K. Ronzano, D. Squires, B. Yost, PharmaSat: drug dose response in microgravity from a free-flying integrated biofluidic/optical culture-and-analysis satellite, in: H. Becker, B.L. Gray (Eds.), *Microfluidics, BioMEMS, and Medical Microsystems IX*, 2011: p. 79290T. <https://doi.org/10.1117/12.881082>.
- [33] C. Kitts, K. Ronzano, R. Rasay, I. Mas, J. Acain, M. Neumann, L. Bica, P. Mahacek, G. Minelli, E. Beck, S. Li, B. Gamp, S. Agnew, J. Shepard, J. Hines, E. Agasid, C. Friedericks, M. Piccini, M. Parra, L. Timucin, C. Beasley, M. Henschke, E. Luzzi, N. Mai, M. McIntyre, R. Ricks, A. Ricco, D. Squires, B. Yost, G. Defouw, A. Schooley, D. Ly, M. Diaz-aguado, E. Stackpole, O. Diaz, T. Doukas, D. Niesel, M. MCGinnis, SSC09-IV-10 Initial Flight Results from the PharmaSat Biological Microsatellite Mission, in: 23rd Annual AIAA/USU Conf on Small Satellites, 2009. <https://doi.org/SSC08-II-4>.
- [34] A.M. Cook, A.L. Mattioda, A.J. Ricco, R.C. Quinn, A. Elsaesser, P. Ehrenfreund, A. Ricca, N.C. Jones, S.V. Hoffmann, The Organism/Organic Exposure to Orbital Stresses (O/OREOS) Satellite: Radiation Exposure in Low-Earth Orbit and Supporting Laboratory Studies of Iron Tetraphenylporphyrin Chloride, *Astrobiology*. 14 (2014) 87–101. <https://doi.org/10.1089/ast.2013.0998>.
- [35] P. Ehrenfreund, A.J. Ricco, D. Squires, C. Kitts, E. Agasid, N. Bramall, K. Bryson, J. Chittenden, C. Conley, A. Cook, R. Mancinelli, A. Mattioda, W. Nicholson, R. Quinn, O. Santos, G. Tahu, M. Voytek, C. Beasley, L. Bica, M. Diaz-Aguado, C. Friedericks, M. Henschke, D. Landis, E. Luzzi, D. Ly, N. Mai, G. Minelli, M. McIntyre, M. Neumann, M. Parra, M. Piccini, R. Rasay, R. Ricks, A. Schooley, E. Stackpole, L. Timucin, B. Yost, A. Young, The O/OREOS mission—Astrobiology in low Earth orbit, *Acta Astronautica*. 93 (2014) 501–508. <https://doi.org/10.1016/j.actaastro.2012.09.009>.
- [36] N.E. Bramall, R. Quinn, A. Mattioda, K. Bryson, J.D. Chittenden, A. Cook, C. Taylor, G. Minelli, P. Ehrenfreund, A.J. Ricco, D. Squires, O. Santos, C. Friedericks, D. Landis, N.C. Jones, F. Salama, L.J. Allamandola, S. V. Hoffmann, The development of the Space Environment Viability of Organics (SEVO) experiment aboard the Organism/Organic Exposure to Orbital Stresses (O/OREOS) satellite, *Planetary and Space Science*. 60 (2012) 121–130. <https://doi.org/10.1016/j.pss.2011.06.014>.
- [37] W.L. Nicholson, A.J. Ricco, E. Agasid, C. Beasley, M. Diaz-Aguado, P. Ehrenfreund, C. Friedericks, S. Ghassemieh, M. Henschke, J.W. Hines, C. Kitts, E. Luzzi, D. Ly, N. Mai, R. Mancinelli, M. McIntyre, G. Minelli, M. Neumann, M. Parra, M. Piccini, R.M. Rasay, R. Ricks, O. Santos, A. Schooley, D. Squires, L. Timucin, B. Yost, A. Young, The O/OREOS Mission: First Science Data from the Space Environment Survivability of Living Organisms (SESLO) Payload, *Astrobiology*. 11 (2011) 951–958. <https://doi.org/10.1089/ast.2011.0714>.
- [38] A. Mattioda, A. Cook, P. Ehrenfreund, R. Quinn, A.J. Ricco, D. Squires, N. Bramall, K. Bryson, J. Chittenden, G. Minelli, E. Agasid, L. Allamandola, C. Beasley, R. Burton, G. Defouw, M. Diaz-Aguado, M. Fonda, C. Friedericks, C. Kitts, D. Landis, M. McIntyre, M. Neumann, M. Rasay, R. Ricks, F. Salama, O. Santos, A. Schooley, B. Yost, A. Young, The O/OREOS Mission: First Science Data from the Space Environment Viability of Organics (SEVO) Payload, *Astrobiology*. 12 (2012) 841–853. <https://doi.org/10.1089/ast.2012.0861>.
- [39] M.R. Padgen, M.P. Lera, M.P. Parra, A.J. Ricco, M. Chin, T.N. Chinn, A. Cohen, C.R. Friedericks, M.B. Henschke, T. V. Snyder, S.M. Spremo, J.-H. Wang, A.C. Matin, EcAMSat spaceflight measurements of the role of σ s in antibiotic resistance of stationary phase *Escherichia coli* in

- microgravity, *Life Sciences in Space Research*. 24 (2020) 18–24. <https://doi.org/10.1016/j.lssr.2019.10.007>.
- [40] M.R. Padgen, T.N. Chinn, C.R. Friedericks, M.P. Lera, M. Chin, M.P. Parra, M.E. Piccini, A.J. Ricco, S.M. Spremo, The EcAMSat fluidic system to study antibiotic resistance in low earth orbit: Development and lessons learned from space flight, *Acta Astronautica*. 173 (2020) 449–459. <https://doi.org/10.1016/j.actaastro.2020.02.031>.
- [41] A.J. Ricco, S.R.S. Maria, R.P. Hanel, S. Bhattacharya, BioSentinel: A 6U Nanosatellite for Deep-Space Biological Science, *IEEE Aerospace and Electronic Systems Magazine*. 35 (2020) 6–18. <https://doi.org/10.1109/MAES.2019.2953760>.
- [42] S.R. Santa Maria, D.B. Marina, S. Massaro Tieze, L.C. Liddell, S. Bhattacharya, BioSentinel: Long-Term *Saccharomyces cerevisiae* Preservation for a Deep Space Biosensor Mission, *Astrobiology*. 20 (2020) ast.2019.2073. <https://doi.org/10.1089/ast.2019.2073>.
- [43] S. Massaro Tieze, L.C. Liddell, S.R. Santa Maria, S. Bhattacharya, BioSentinel: A Biological CubeSat for Deep Space Exploration, *Astrobiology*. 20 (2020) ast.2019.2068. <https://doi.org/10.1089/ast.2019.2068>.
- [44] J. Park, M.L. Salmi, W.W.A. Wan Salim, A. Rademacher, B. Wickizer, A. Schooley, J. Benton, A. Cantero, P.F. Argote, M. Ren, M. Zhang, D.M. Porterfield, A.J. Ricco, S.J. Roux, J.L. Rickus, An autonomous lab on a chip for space flight calibration of gravity-induced transcellular calcium polarization in single-cell fern spores, *Lab on a Chip*. 17 (2017) 1095–1103. <https://doi.org/10.1039/C6LC01370H>.
- [45] E.D. Fleming, B.M. Bebout, M.X. Tan, F. Selch, A.J. Ricco, Biological system development for GraviSat: A new platform for studying photosynthesis and microalgae in space, *Life Sciences in Space Research*. 3 (2014) 63–75. <https://doi.org/10.1016/j.lssr.2014.09.004>.
- [46] C. Giagkoulovits, B.C. Cheah, M.A. Al-Rawhani, C. Accarino, C. Busche, J.P. Grant, D.R.S. Cumming, A 16 x 16 CMOS Amperometric Microelectrode Array for Simultaneous Electrochemical Measurements, *IEEE Trans. Circuits Syst. I*. 65 (2018) 2821–2831. <https://doi.org/10.1109/TCSI.2018.2794502>.
- [47] Y. Zhang, Y. Zhao, R. Lv, A review for optical sensors based on photonic crystal cavities, *Sensors and Actuators A: Physical*. 233 (2015) 374–389. <https://doi.org/10.1016/j.sna.2015.07.025>.
- [48] S.Yu. Gorbunova, A.L. Avsiyan, Diurnal dynamics of green microalga *Tetraselmis viridis* culture density in open pond monitored by optical density sensor, *Bioresource Technology Reports*. 20 (2022) 101251. <https://doi.org/10.1016/j.biteb.2022.101251>.
- [49] I. Mihai, F. Addiego, D. Ruch, V. Ball, Composite and free standing PANi-PVA membranes as flexible and stable optical pH sensors, *Sensors and Actuators B: Chemical*. 192 (2014) 769–775. <https://doi.org/10.1016/j.snb.2013.11.042>.
- [50] J. Posseckardt, C. Schirmer, A. Kick, K. Rebatschek, T. Lamz, M. Mertig, Monitoring of *Saccharomyces cerevisiae* viability by non-Faradaic impedance spectroscopy using interdigitated screen-printed platinum electrodes, *Sensors and Actuators B: Chemical*. 255 (2018) 3417–3424. <https://doi.org/10.1016/j.snb.2017.09.171>.
- [51] J. Paredes, S. Becerro, S. Arana, Comparison of real time impedance monitoring of bacterial biofilm cultures in different experimental setups mimicking real field environments, *Sensors and Actuators B: Chemical*. 195 (2014) 667–676. <https://doi.org/10.1016/j.snb.2014.01.098>.
- [52] S. Kim, J.-H. Han, B. Chua, J.J. Pak, A pH Sensing Pipette for Cross-Contamination Prevention in Industrial Fermentation, *IEEE Transactions on Industrial Electronics*. 69 (2022) 7461–7469. <https://doi.org/10.1109/TIE.2021.3099251>.
- [53] L. Li, A.V. Zhdanov, D.B. Papkovsky, Advanced multimodal solid-state optochemical pH and dual pH/O₂ sensors for cell analysis, *Sensors and Actuators B: Chemical*. 371 (2022) 132486. <https://doi.org/10.1016/j.snb.2022.132486>.

- [54] P. Yu, G.S. Wilson, An independently addressable microbiosensor array: What are the limits of sensing element density?, *Faraday Disc.* 116 (2000) 305–317. <https://doi.org/10.1039/b001611j>.
- [55] M. Sophocleous, J.K. Atkinson, A review of screen-printed silver/silver chloride (Ag/AgCl) reference electrodes potentially suitable for environmental potentiometric sensors, *Sensors and Actuators A: Physical.* 267 (2017) 106–120. <https://doi.org/10.1016/j.sna.2017.10.013>.
- [56] C. Clark, R. Logan, *Power Budgets for Mission Success*, (2011).
- [57] GL55 Series Photoresistor Datasheet, (2016) 1–5.
- [58] N. Coote, B.H. Kirsop, FACTORS RESPONSIBLE FOR THE DECREASE IN pH DURING BEER FERMENTATIONS, *Journal of the Institute of Brewing.* 82 (1976) 149–153. <https://doi.org/10.1002/j.2050-0416.1976.tb03739.x>.
- [59] W.W. Wan Salim, J. Park, A. Haque, D. Porterfield, Lab-on-a-Chip Approaches for Space-Biology Research, *Recent Patents on Space Technology.* 3 (2013) 24–39. <https://doi.org/10.2174/18776116112029990010>.
- [60] Korent, A., Žagar Soderžnik, K., Šturm, S., & Žužek Rožman, K. (2020). A Correlative Study of Polyaniline Electropolymerization and its Electrochromic Behavior. *Journal of The Electrochemical Society*, 167(10), 106504. <https://doi.org/10.1149/1945-7111/ab9929>
- [61] Wang, Y., Xu, J., Zong, W., & Zhu, Y. (2011). Enhancement of photoelectric catalytic activity of TiO₂ film via Polyaniline hybridization. *Journal of Solid State Chemistry*, 184(6), 1433–1438. <https://doi.org/10.1016/j.jssc.2011.04.001>
- [62] De Azevedo, W.M., A.P. Da Costa Lima, and E.S. De Araujo. “Radiation Induced Effects on Electrical Properties of Polyaniline.” *Radiation Protection Dosimetry* 84, no. 1 (August 1, 1999): 77–82. <https://doi.org/10.1093/oxfordjournals.rpd.a032802>.